nature synthesis

Article

https://doi.org/10.1038/s44160-024-00726-y

Helical protein nanotubules assembled from sacrificial supramolecular polymers

Received: 1 September 2024

Accepted: 16 December 2024

Published online: 16 January 2025

Check for updates

Linfei Ye[1], Xiaoduo Dong[1], Chong Wang[2], Yao Lin[3], Myongsoo Lee[4], Long Li[1] ✉ & Guosong Chen[1] ✉

Precise helical supramolecular polymers of proteins can only be achieved in vivo by tuning complex, competing supramolecular interactions. This formation suggests a level of cellular control that defines functional structures with high fidelity. Achieving such a phenomenon through synthetic reactions is a challenge owing to the lack of native competing interactions. Here we report that synthetic self-assembled polymers spontaneously disassemble to trigger helical growth of protein units to form well-defined protein tubules in vitro. Cryogenic electron microscopy reconstruction at near-atomic resolution reveals uniform protein helical arrays rather than polymorphic arrays. These uniform arrays are similar to natural microtubules, and the aggregated structure of the sacrificed supramolecular ligands within the protein nanotubule is pentameric. The formation of the protein nanotubules, rather than supramolecular polymer of ligands, regulates the physical properties of the solution and the morphology of liposomes. It was shown that enthalpy–entropy compensation provided by the dissociation of aggregated ligands modulates the homogeneity of the helical pattern of the protein nanotubules, shedding light on the creation of sophisticated bionic materials.

Nature exploits the complex interplay of supramolecular interactions to construct highly organized hierarchical architectures with regulated functions[1,2]. Notably, biological supramolecular polymers with high aspect ratios—such as flagella[3], microtubules[4,5] and microfilaments[6]—are ubiquitous in organisms from prokaryotes to eukaryotes, providing special material properties for living systems. These supramolecular polymers normally have uniform helical packing of protein building blocks, suggesting that one level of cellular control involves defining unique linear geometries. For example, the uniform 13-fold symmetry of microtubules is preferred in vivo although polymorphism can be easily found in vitro from purified tubulin[7]. Such uniform supramolecular packing ensures functional fidelity, which is further tuned by other one-dimensional assemblies of molecules located at regulatory nodes, providing alternative facets of function regulation within the cell[8,9]. In living cells, the dynamic formation of microtubules can be regulated by an competitive network of microtubule-associated proteins (MAPs) that stabilize microtubules[10,11], providing a well-balanced system under physiological conditions[12] (Fig. 1a). By such sophisticated interactions of different assemblies in competitive balance, the biological system is precisely and exquisitely regulated to maintain correct functioning, where errors can be efficiently detected and fixed[13,14].

Over the past decades, synthetic molecules[15,16], inorganic particles[17,18] and engineered biomacromolecules[19–21] have been used to build artificial supramolecular polymers to mimic the unique structures and functions of native linear assemblies, providing a promising class of advanced materials and an avenue to unravel the molecular

[1]State Key Laboratory of Molecular Engineering of Polymers and Department of Macromolecular Science, Fudan University, Shanghai, China. [2]Shanghai Xuhui Central Hospital, Zhongshan-Xuhui Hospital, and the Shanghai Key Laboratory of Medical Epigenetics, the International Co-laboratory of Medical Epigenetics and Metabolism (Ministry of Science and Technology), Institutes of Biomedical Sciences, Fudan University, Shanghai, China. [3]Polymer Program, Institute of Materials Science and Department of Chemistry, University of Connecticut, Storrs, CT, USA. [4]Department of Chemistry, Shanghai Key Laboratory of Molecular Catalysis and Innovative Materials, Fudan University, Shanghai, China. ✉e-mail: long_li@fudan.edu.cn; guosong@fudan.edu.cn

mechanisms of relevant physiological phenomena[22,23]. The cellular non-covalent interaction networks for regulating biological supramolecular polymers with structural homogeneity have inspired research on artificial supramolecular polymers that comprise competitive interactions, which, as far as we know, are only based on the synthetic molecules[24,25]. For example, a supramolecular system containing surfactants and supramolecular monomers was developed, in which the competitive network resulted in sol–gel transition upon dilution[26]. However, the competitive interplay has not been explored in supramolecular polymerization of biomacromolecular building blocks, owing to the challenges in introducing competitive supramolecular polymers with native sophisticated regulation for homogeneity control[27,28].

Here we construct a multicomponent competitive system containing supramolecular polymers of small molecules and biomacromolecules (Fig. 1b). The proteins can be induced to polymerize into helical nanotubules (with high structural similarity to natural microtubules) by tetratopic ligands, which themselves can self-assemble into nanofibres. By molecular design, the robustness of the ligand supramolecular polymer (LSP) was regulated to compete with the protein supramolecular polymer (PSP), enabling well-regulated pathways and outcomes of multicomponent supramolecular polymer systems. This results in five nanotubules with variable surface lattices, protofilament numbers, helical pitches and tube diameters. These findings suggest that, after binding with proteins, sacrifice of ligand assemblies with varying robustness provided a distinct pathway that was driven by entropy instead of enthalpy, which means the formation of LSPs before complexation with protein can modulate the formation rate and homogeneity of the PSPs. Although helical tubes based on soybean agglutinin (SBA) have been reported[28], such competition has never been achieved before with ligands in the monomeric state. Importantly, the different outcomes affected the physical properties of the competitive system, enabling modulation of viscosity by the dominant supramolecular polymer. Furthermore, this system was employed to regulate the morphology of vesicles in confined space. These findings provide an alternative way to understand the thermodynamic origins and interplay networks underlying the biological supramolecular polymers. They also offer an approach for the design and precise control of desirable properties via interactive supramolecular structures. This provides a potential basis for the creation of bionic materials and artificial intelligent materials.

Designing LSP for protein nanotubules

A class of ligand structures with certain aggregation tendency and structural rigidity is required to construct the sacrificial ligands that can disassemble from their own supramolecular polymers to generate protein nanotubules (Fig. 2a). Here, pyrenes (P) were employed as hydrophobic cores, considering their tendency for π–π interactions[29,30], which was further enhanced by tetraphenyl extension. The native ligand of SBA, D-galactoside (Gal), was coupled with the hydrophobic core by one ethylene glycol linker (E_1), named **PE_1Gal**. Meanwhile, additional ethylene glycol linkers (E_2) were designed to modulate the aggregation state of the hydrophobic core, thereby obtaining another ligand **PE_2Gal** (Fig. 2a and Supplementary Figs. 1–8). With the ligands in hand, we investigated their critical micelle concentration (Supplementary Fig. 9). The results showed that changes in fluorescent spectra of these two ligands at different concentrations were similar. Moreover, when the concentrations were higher than 0.1 μM, a new peak assigned to aggregated species emerged at 540 nm, supporting that the concentrations in subsequent experiments (maintained at 160 μM) were above their critical micelle concentration. The ultraviolet spectra of the two ligands in DMSO exhibited a hypsochromic shift, which also indicated the formation of assemblies in aqueous solution (Supplementary Fig. 10). The observation of cryogenic electron microscopy (cryo-EM) showed that both ligands assembled into fibrous structures with a width of approximately 2 nm (Fig. 2g,h), indicating the formation of LSP via π–π stacking of the hydrophobic core.

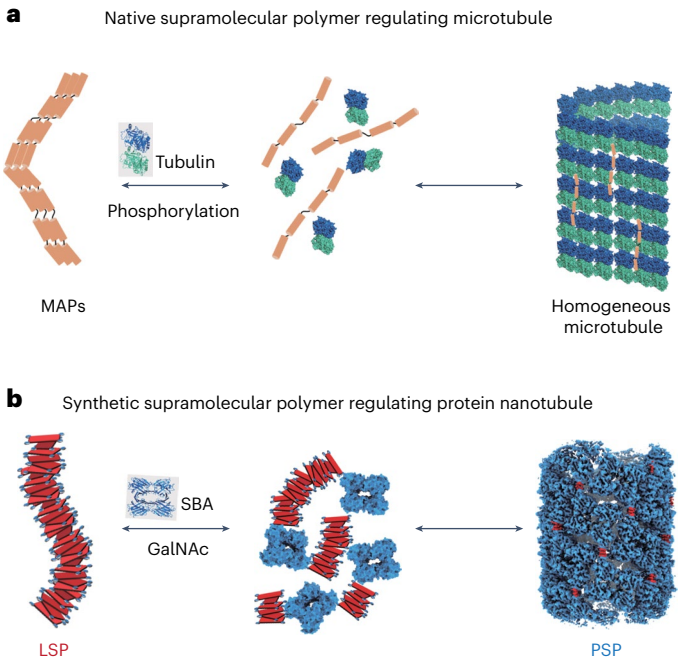

Fig. 1 | Design of the sacrificial supramolecular polymer for protein supramolecular polymerization. a, Schematic illustration of sacrificial MAPs in nature. **b**, Schematic illustration of sacrificial LSP that regulates PSP.

Interestingly, it was found that these molecules had different chiralities despite the same D-Gal being modified onto their backbones. The circular dichroism spectra results showed that, for **PE_1Gal**, obvious chiral signals were observed at 325 nm and 378 nm, which were related to its chromophore, indicating the formation of chiral supramolecular structures (Fig. 2b and Supplementary Fig. 11). This signal may be explained by the chiral environment provided by the aggregated D-Gal derivative on the non-chiral hydrophobic core via the stacking into LSP[31]. However, no substantial Cotton effect was observed for **PE_2Gal** (Fig. 2b). The achiral phenomenon indicated that although the two ligands exhibited similarly fibrous structures, the molecular packing of **PE_2Gal** can be very different from that of **PE_1Gal**. An all-atom molecular dynamics simulation was therefore employed to investigate the structural differences. The results revealed that the molecular packing of **PE_2Gal** was not as condensed as those of **PE_1Gal** (Fig. 2c). Compared with **PE_1Gal**, the cluster of **PE_2Gal** has a higher average distance between the geometric centres of pyrene and the solvent-accessible surface area (SASA) (Fig. 2d and Supplementary Figs. 12 and 13), implying a relatively unstable LSP. The hydrogen/deuterium exchange mass spectrometry results consistently showed that the active hydrogens in LSP of **PE_2Gal** were replaced by deuterium more rapidly than that of **PE_1Gal** (Supplementary Fig. 14), further confirming the different robustness of the two fibrous structures.

Competition between LSP and PSP drives liposome deformation

Encouraged by the successful generation of LSP, we investigated the competition between LSP and PSP by incubating the ligands with SBA—a homotetramer with four Gal-binding sites—in HEPES buffer (see Methods for details). After mixing, the Tyndall effect was enhanced in **PE_2Gal/SBA**, whereas **PE_1Gal/SBA** showed no obvious changes, indicating that there was a substantial difference in the ability of the two LSPs to induce protein self-assembly (Supplementary Fig. 15). This difference was further verified by cryo-EM. It was observed that PSP was generated with the disappearance of the **PE_2Gal** LSP (Fig. 2h). Meanwhile, fitting of small-angle X-ray scattering (SAXS) data revealed a tubular structure with an inner diameter of 16 nm and a wall thickness

https://doi.org/10.1038/s44160-024-00726-y

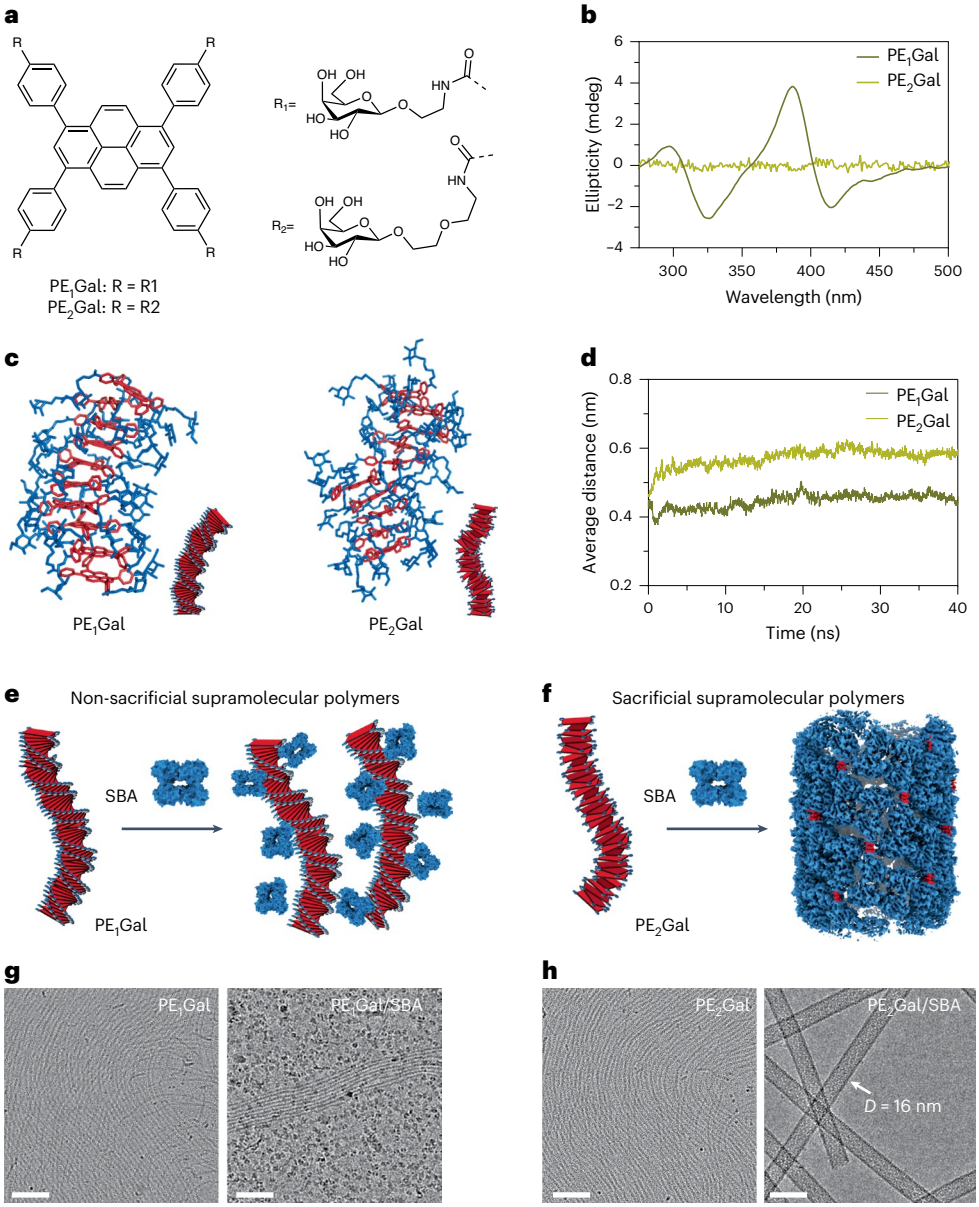

Fig. 2 | Design and analysis of the LSPs for protein nanotubules. a, Molecular structures of ligands **PE_1Gal** and **PE_2Gal** with pyrene cores and distinct ethylene glycol linkers. **b**, Circular dichroism spectra of **PE_1Gal** and **PE_2Gal** (160 μM) at room temperature; the path length of the cell is 1 mm. **c**, Molecular dynamics simulates the condensed arrangement of **PE_1Gal** and the loose arrangement of **PE_2Gal** in aqueous solution. **d**, Calculation of the average distance between the geometric centres of pyrenes within **PE_1Gal** and **PE_2Gal**. All of the simulations described above were performed using GROMACS 2018 (ref. 45). **e**,**f**, Schematic illustration of non-sacrificial **PE_1Gal** (**e**) and sacrificial **PE_2Gal** assembled with proteins (**f**). **g**,**h**, Cryo-EM images of **PE_1Gal** (**g**) and **PE_2Gal** (**h**), presented as fibril structures at 160 μM in aqueous solution, and their assembled behaviour after the addition of 20 μM SBA. *D* represents the diameter of protein nanotubule which is 16 nm. Scale bar, 20 nm.

of 4 nm, which was consistent with the cryo-EM results (Fig. 2h and Supplementary Fig. 16). By contrast, **PE_1Gal** failed to induce formation of regular protein assemblies (Fig. 2g and Supplementary Fig. 16). Based on 300 kV cryo-EM, the structure of **PE_2Gal/SBA** was obtained with 3.57 Å resolution (Fig. 3a). The three-dimensional (3D) reconstruction result showed that the tubular structure encompassed the central pore with a diameter of ~13 nm surrounded by a single layer of SBA with a thickness of ~4 nm. This protein nanotubules consisted of a quadruple helix of SBA, with each helical turn comprising six SBA tetramers (denoted 6–4). More importantly, the high-resolution density map allowed us clearly observe ligand arrangement within the protein nanotubule. The results suggested that the **PE_2Gal** ligands were arranged as pentamers between the four adjacent proteins (Fig. 3b). The ligand molecules in this pentamer form a π-conjugation plane perpendicular to the tubular surface, whereas the **PE_2Gal** ligands were stacked via π–π interactions to form a stable pentameric supramolecular aggregate. As for the pentamer, the first and fifth **PE_2Gal** molecules were connected to the surrounding two SBAs with two of their Gal, respectively (Fig. 3b and Supplementary Fig. 17). Each SBA tetramer interacts with one pentamer at their four carbohydrate-binding sites (Supplementary Fig. 17). The LSP of **PE_2Gal** dissociated into a pentameric form in the protein nanotubule, confirming the competition of supramolecular polymerization between the ligand and the protein, where the LSP sacrificed to form PSP.

To confirm this competition, circular dichroism was used to investigate the changes of the two LSPs while the same amount of SBA was introduced. The results indicated that the formation of protein assemblies was inversely correlated to the chirality of the aggregated ligands.

https://doi.org/10.1038/s44160-024-00726-y

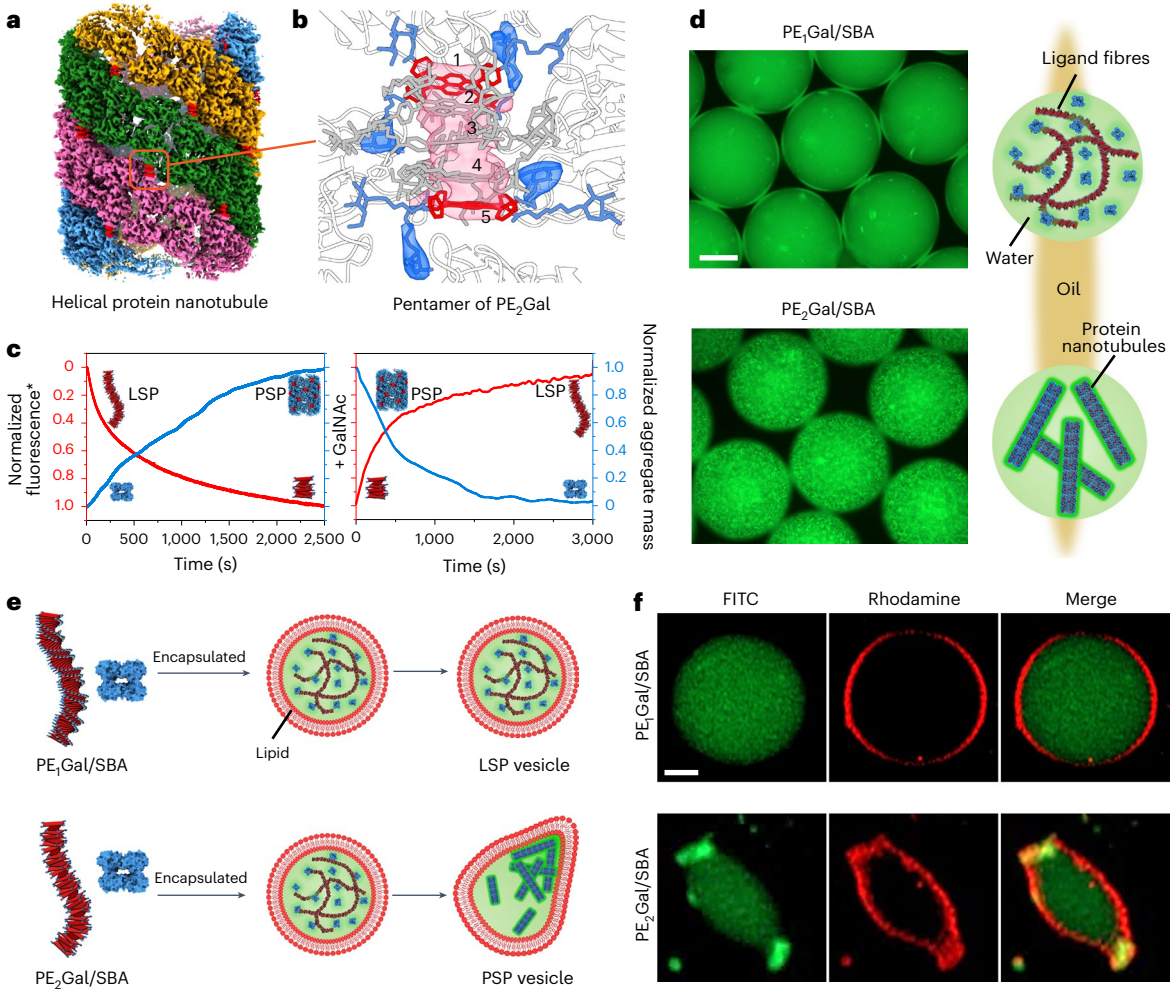

Fig. 3 | PSP induced by PE_2Gal and the competition effect among them. **a**, Electron density map of nanotubules induced by **PE_2Gal** through three-dimensional reconstruction. The different protofilaments are coloured blue, pink, green and yellow. **b**, A magnified view of the **PE_2Gal** structural model fitted into an electron density map. The hydrophobic core of pyrene is demonstrated by the electron density coloured red, whereas the four Gal groups binding to the four SBAs are indicated by the electron density coloured blue. **c**, Characterization and schematic representation of competition between LSP and PSP in the case of **PE_2Gal**. Normalized fluorescence intensity of ligand (red) and light-scattering data of protein assembly (blue) during reversible competition. [ligand] = 160 μM, [SBA] = 20 μM, [GalNAc] = 640 μM. *The curve of LSP fluorescence intensity over time is inverted along the *x* axis to represent the competitive trends. **d**, Confocal images of the **PE_1Gal/SBA** and **PE_2Gal/SBA** encapsulated into droplets using microfluidics. Scale bar, 10 μm. **e**,**f**, A schematic diagram showing the use of liposomes encapsulating **PE_1Gal/SBA** and **PE_2Gal/SBA** (**e**), and the result of confocal fluorescence images (**f**). The green channel represents SBA proteins labelled with FITC, whereas the red channel represents lipids labelled with rhodamine. Scale bar, 2 μm.

For **PE_2Gal**, which originally exhibited no chiral peaks, the negative signals appeared at 320 nm and 420 nm, which were enhanced with increasing concentrations of SBA (Supplementary Fig. 19). This suggests that the ligand was influenced by the chiral environment provided by the protein. For **PE_1Gal**, which cannot induce protein self-assembly, there was no change in the circular dichroism spectrum, indicating that the added SBA had a negligible effect on this robust LSP (Supplementary Fig. 19). Furthermore, the time-tracking of this competition process was investigated via fluorescent spectroscopy and light scattering, which showed that the fluorescence intensity of **PE_2Gal** increased substantially when SBA was added, indicating the dissociation of **PE_2Gal** LSP. Meanwhile, tracking of scattered light intensity revealed the generation of PSP (Fig. 3c). These results suggested that, for **PE_2Gal/SBA**, the interaction between the **PE_2Gal** pentamer is much weaker than that between the pentamer and SBA. However, for **PE_1Gal/SBA**, the competition between the two types of supramolecular polymers did not take place. The fluorescence intensity of **PE_1Gal** barely changed, indicating the stability of this robust nanofibre. Meanwhile, negligible changes in scattered light intensity implied that the protein did not form aggregates (Supplementary Fig. 20). Together with the cryo-EM observations and molecular dynamics simulations of the initial fibrous structures of the two ligands and their assembly process after binding SBA (Supplementary Figs. 21 and 22), these results demonstrate that although similar LSPs were observed from both of the ligands, the relatively loose packing of **PE_2Gal** facilitated the formation of PSPs via supramolecular competition. By contrast, **PE_1Gal**, with its condensed packing, did not. These results suggest that, compared with **PE_2Gal**, the Gal interactive site of **PE_1Gal** is closer to the hydrophobic core, which reduces the degree of conformational freedom, resulting in lower entropy loss and easier self-association to form LSP. This is further verified by the small-angle neutron scattering experiments that **PE_1Gal** has a pronounced periodic alignment peak, whereas **PE_2Gal** does not (Supplementary Fig. 23). However, this lack of conformational freedom might hinder the formation of complexes with SBA. When the binding ability of **PE_1Gal** or **PE_2Gal** as fibrous structure to SBA was measured, it was found that **PE_2Gal** was able to bind to SBA, whereas **PE_1Gal** did not exhibit such affinity (Supplementary Fig. 24). As a result, there is a correlation between self-assembly capability and complexation

capability with SBA, that is, the ability of LSP self-assembly is inversely related to that of PSP generation.

Considering that the formation of nanotubules and the decomposition of fibrous structures primarily depend on the interactions between Gal and SBA—which can be competitively substituted by the stronger binding of *N*-acetylgalactosamine (GalNAc) to SBA[32]—we investigated the reversibility of the competition process by adding GalNAc to **PE_2Gal/SBA**. The decrease of scattered light intensity suggests disassembly of the PSP. Meanwhile, the decrease of ligand fluorescence intensity indicated that **PE_2Gal** pentamers were released from the PSP and repolymerized into LSP (Fig. 3c and Supplementary Fig. 25). Diffusing-wave spectroscopy (DWS) was used to investigate the microrheological properties of the solutions, since the competition between such supramolecular polymers may tune the property of their solution. The results revealed that the viscosity of LSP and SBA were only around 10^{-2} Pa s. By contrast, the viscosity of **PE_2Gal/SBA** reached 10^{-1} Pa s, which is one magnitude higher, suggesting that the transformation from LSP to PSP resulted in changes in the properties of the system (Supplementary Fig. 26). Following the addition of GalNAc, a decrease in viscosity was observed as the protein nanotubules dissociated and the LSP reorganized, thereby reversing the competitive behaviour (Supplementary Fig. 26). For **PE_1Gal/SBA**, such a dramatic change in viscosity was not observed, as the competition between the two types of supramolecular polymers did not take place (Supplementary Fig. 27).

Such competition was investigated within simplified models of the confined space inside cells. Here, droplets with a diameter of 30 μm were fabricated using microfluidic techniques, encapsulating two LSPs and each assembly with protein. The localized brightening observed in the confocal images—owing to fluorescein isothiocyanate (FITC)-labelled SBA aggregation—indicated that **PE_2Gal** can induce PSP formation (Fig. 3d). However, the homogeneous fluorescence image of **PE_1Gal/SBA** suggested that no protein nanotubule forms were present. Furthermore, liposomes 5 μm in diameter were employed to encapsulate the two LSPs and SBA (Fig. 3e). The results demonstrated that the successful growth of protein nanotubules led to the deformation of the liposome in the **PE_2Gal/SBA** scenario (Fig. 3f), which was dramatically different from the **PE_1Gal/SBA** scenario—in which PSP competition was absent—where the liposomes maintained their spherical shape. This was confirmed by quantitative analyses of the extend of liposome deformation over time and comparative studies of assemblies released from liposome (Supplementary Figs. 28 and 29). The deformation of the liposomes may be attributed to the interaction between the nanotubules and lipid bilayer (Supplementary Fig 30). These results indicated that the ligand-induced protein nanotubule provides an alternative approach to deform liposomes. Together, these results demonstrated that the properties of the multi-component competitive system containing supramolecular polymers of small molecules and biomacromolecules can be remarkably regulated by the different competitive outcomes between the two components.

Regulating protein nanotubules by ligand aggregation

The successful outcomes of the competition between two types of LSPs suggest that modulating ligand aggregation is an unexplored route to controlling the formation of protein nanotubules. We therefore synthesized an extended series of four-armed ligands, each with different hydrophobic cores to provide diverse aggregation tendencies (Fig. 4a). Three hydrophobic cores, pyrazine (**Z**), benzene (**B**) and tetraphenylbenzene (**TB**) were coupled with Gal, and extended with the tetraphenyl and ethylene glycol linker. This resulted in four new ligands: **ZE_1Gal**, **BE_1Gal**, **TBE_1Gal** and **TBE_2Gal** (Supplementary Figs. 31–38). Molecular dynamics results showed that **ZE_1Gal** and **BE_1Gal** had weak aggregation tendencies, which was confirmed by the decreases in SASA; on the other hand, substantial increases in SASA indicated that **TBE_1Gal** and **TBE_2Gal** displayed strong aggregation tendencies (Supplementary Fig. 39). A comprehensive understanding of the aggregation ability of the ligands in aqueous solution (concentration = 160 μM) was provided by the combination of different characterization techniques. Cryo-EM observation revealed that **ZE_1Gal** and **BE_1Gal** had no obvious aggregates, whereas **TBE_1Gal** and **TBE_2Gal** self-assembled into layered structures with regular lattice and fibrous assemblies, respectively (Supplementary Fig. 40). For **ZE_1Gal** and **BE_1Gal**, the aggregation states and sizes were confirmed by fluorescence spectra and SAXS. Consistent with the cryo-EM results, the emission of **ZE_1Gal** remained unchanged as the ligand concentration changed, indicating that **ZE_1Gal** existed in the form of monomers in water (Supplementary Fig. 41). This was confirmed by the radius of gyration (R_g) of 0.75 nm in aqueous solution (Supplementary Figs. 42 and 43). Yet, when the concentration was increased to 0.1 μM, a hypsochromic shift of the fluorescent emission was observed in **BE_1Gal**, suggesting that this ligand exhibited aggregation[33] (Supplementary Fig. 41). Moreover, the R_g measured by SAXS was about 1.3 nm, which confirmed that **BE_1Gal** existed as oligomers in water rather than monomers (Supplementary Figs. 42 and 43). The diffusion-ordered ^{1}H NMR spectroscopy showed that the diffusion coefficient of **ZE_1Gal** (2×10^{-10} m^2 s^{-1}) was twice of that of **BE_1Gal** (1×10^{-10} m^2 s^{-1}), suggesting that **BE_1Gal** aggregated in aqueous solution, whereas **ZE_1Gal** did not (Supplementary Fig. 44). Together, combining with the observations of the ligands **PE_1Gal** and **PE_2Gal**, these results indicated the order of aggregation tendencies for the six ligands, namely, the aggregation ability from weak to strong could be **ZE_1Gal**, **BE_1Gal**, **PE_2Gal**, **PE_1Gal**, **TBE_2Gal** and **TBE_1Gal** (Fig. 4b).

After incubating the ligands with SBA, the supramolecular polymerization of proteins was influenced by the aggregation of the ligands. The circular dichroism spectra results showed that **ZE_1Gal** and **BE_1Gal** exhibited obvious chiral peaks at 320 nm after adding SBA (Supplementary Fig. 45), similar to **PE_2Gal**, which was attributed to the ligands entering the chiral environment of the protein, suggesting the generation of protein nanotubules. The cryo-EM and SAXS results confirmed the structure of these protein nanotubules (Supplementary Fig. 46). The diameters of **ZE_1Gal/SBA** and **BE_1Gal/SBA** were approximately 30 nm and 35 nm, respectively. While, for **TBE_1Gal** and **TBE_2Gal**, which were similar to **PE_1Gal**, no substantial changes in circular dichroismpeaks and SAXS signals were observed (Supplementary Figs. 45 and 46). It was confirmed that the two assembled ligands maintained their stability after adding proteins, and the protein nanotubules could not be generated owing to the strong robustness of supramolecular architectures of **TBE_1Gal** and **TBE_2Gal**.

3D reconstruction was employed to further investigate these tubular structures (Fig. 4c–f and Supplementary Fig. 47). The two-dimensional class averaging results showed that, for **ZE_1Gal** existing as a monomer in water, the assemblies contained three types of protein nanotubules with different inner diameters of 33.8 nm (28%), 29.1 nm (32%) and 23.9 nm (40%), respectively. Meanwhile, the central *Z*-section view and the reconstructed density maps showed that, in these polymorphic architectures, the periodic structures were composed of seven-, six-, and four-fold helical strands, each containing 12, 11 and 10 SBA tetramers as a cycle (referred as 12–7, 11–6 and 10–4), respectively. Although, for ligands that existed in the form of oligomers in water, similar to **PE_2Gal/SBA** (6–4), **BE_1Gal/SBA** was uniform protein nanotubules with an inner diameter of 23.4 nm, and the periodic structure consisted of three-fold helical strands containing 9 tetrameric SBA as a cycle (9–3). It is worth mentioning that, the diameter and helical pitch of different nanotubules fitted well with the surface lattice accommodation model[28] (Supplementary Fig. 48). Furthermore, the 3D reconstructions showed that, although **ZE_1Gal/SBA** was polymorphic, the ligand existed as monomers in all three tubular structures, and each ligand was connected to four SBA tetramers by four Gal groups on four arms. For the uniform protein nanotubules of **BE_1Gal/SBA**, the connection between ligand and protein was observed in the same

https://doi.org/10.1038/s44160-024-00726-y

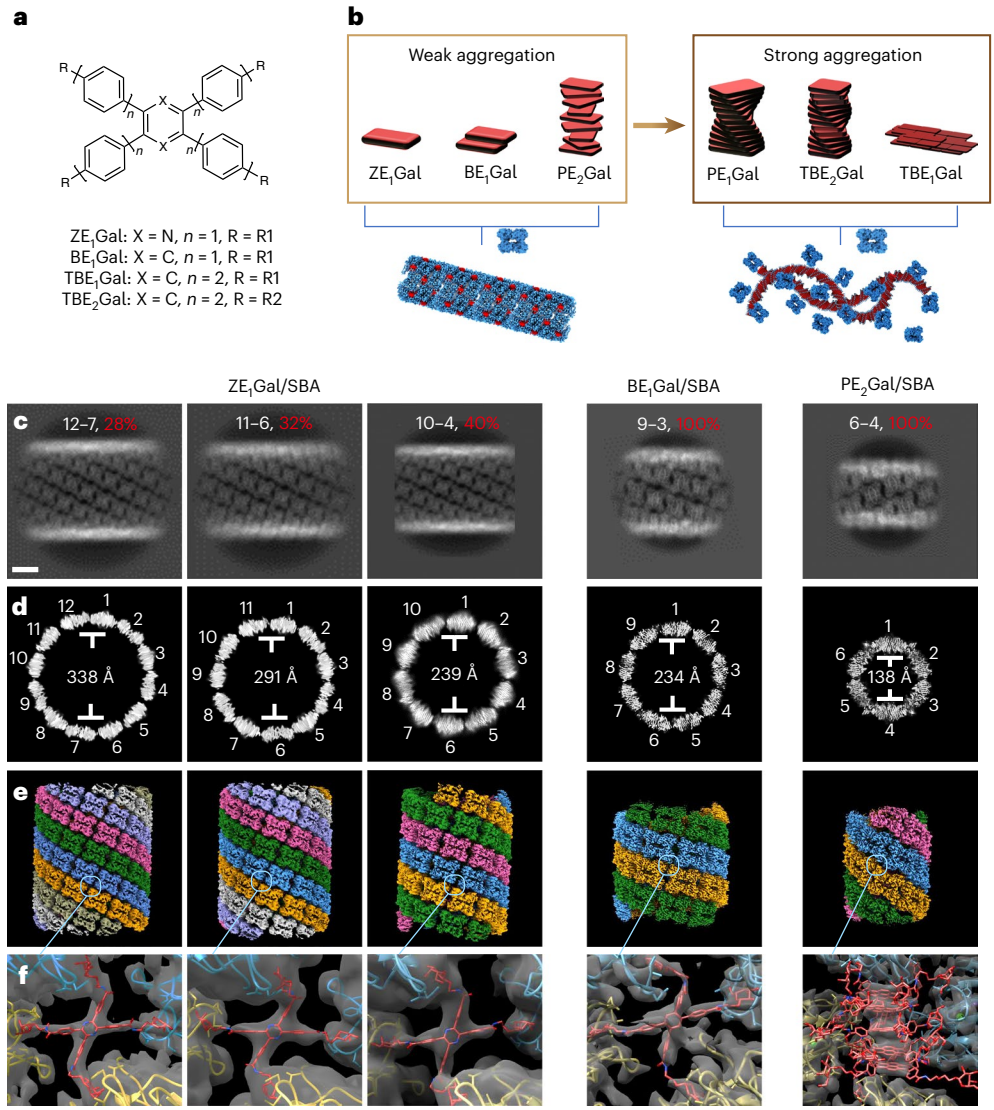

Fig. 4 | Extended ligands design and molecular model for nanotubules. **a**, The molecular structure of extended ligands with different hydrophobic cores. **b**, A schematic illustrating the different aggregation trends of six ligands and whether they can induce PSP. **c**, 3D reconstruction of different nanotubules. Reference-free 2D class averages calculated from single-particle cryo-EM micrographs. **d**, Central *Z*-sections of the reconstructed density map of protein nanotubules. **e**, Electron density map of protein nanotubules after 3D reconstruction. The different protofilaments are uniquely coloured. **f**, Close view of the structural model of SBA and ligands fitted in an electron density map. The labels at the top of panels **c** represent the types of nanotubules and their corresponding percentage in solution. For example, '6–4, 100%' at the top of the **PE_2Gal/SBA** column indicates that 100% of tubes have four longitudinal protofilaments, and each helix has six SBA tetramers. Scale bar, 10 nm.

manner as **ZE_1Gal/SBA**. Considering the oligomeric state of **BE_1Gal** in aqueous solution, it indicated the dissociation of ligand aggregates to generate PSP, which could be similar to that of **PE_2Gal/SBA**.

Competition controls kinetics and homogeneity of PSP

To investigate the differences between polymorphic and homogeneous protein nanotubules, the kinetics of the protein supramolecular polymerization induced by **ZE_1Gal, BE_1Gal** and **PE_2Gal** were tracked by SAXS. For **ZE_1Gal/SBA**, the characteristic peaks of a tubular structure confirmed that the protein supramolecular polymerization occurred at 5 min and reached equilibrium within 30 min (Fig. 5a). For **BE_1Gal**-induced protein supramolecular polymerization, the SAXS signal increased within 30 min and equilibrated until 8 h (Fig. 5b), whereas equilibrium was not observed in **PE_2Gal/SBA** even after 24 h (Fig. 5c). The formation of protein nanotubules induced by **PE_2Gal/SBA** was also characterized by circular dichroism, which was consistent with the SAXS results (Supplementary Fig. 49). Combining with the aggregation states of the ligands, it suggested that the rate at which the protein polymerized into nanotubules decreased with the enhanced aggregation of the ligand; that is, stronger competition between the ligands and SBA resulted in a slower rate of protein microtubule production. In the non-competitive process, the fluorescence intensity of **ZE_1Gal** did not change substantially, indicating that this ligand maintained its monomeric state during protein supramolecular polymerization (Fig. 5d). By contrast, after adding SBA, the fluorescence intensity of oligomeric **BE_1Gal** increased slightly owing to the reduction of aggregation-induced quenching[34], indicating that its oligomers dissociated into monomers. The increase of the fluorescence intensity was observed in **PE_2Gal/SBA**, in which the ligand dissociated from supramolecular nanofibres into pentamers in protein nanotubules. These results were consistent with the ligand structure deciphered by high-resolution reconstruction (Fig. 4f), revealing the existence of different supramolecular competition pathway.

https://doi.org/10.1038/s44160-024-00726-y

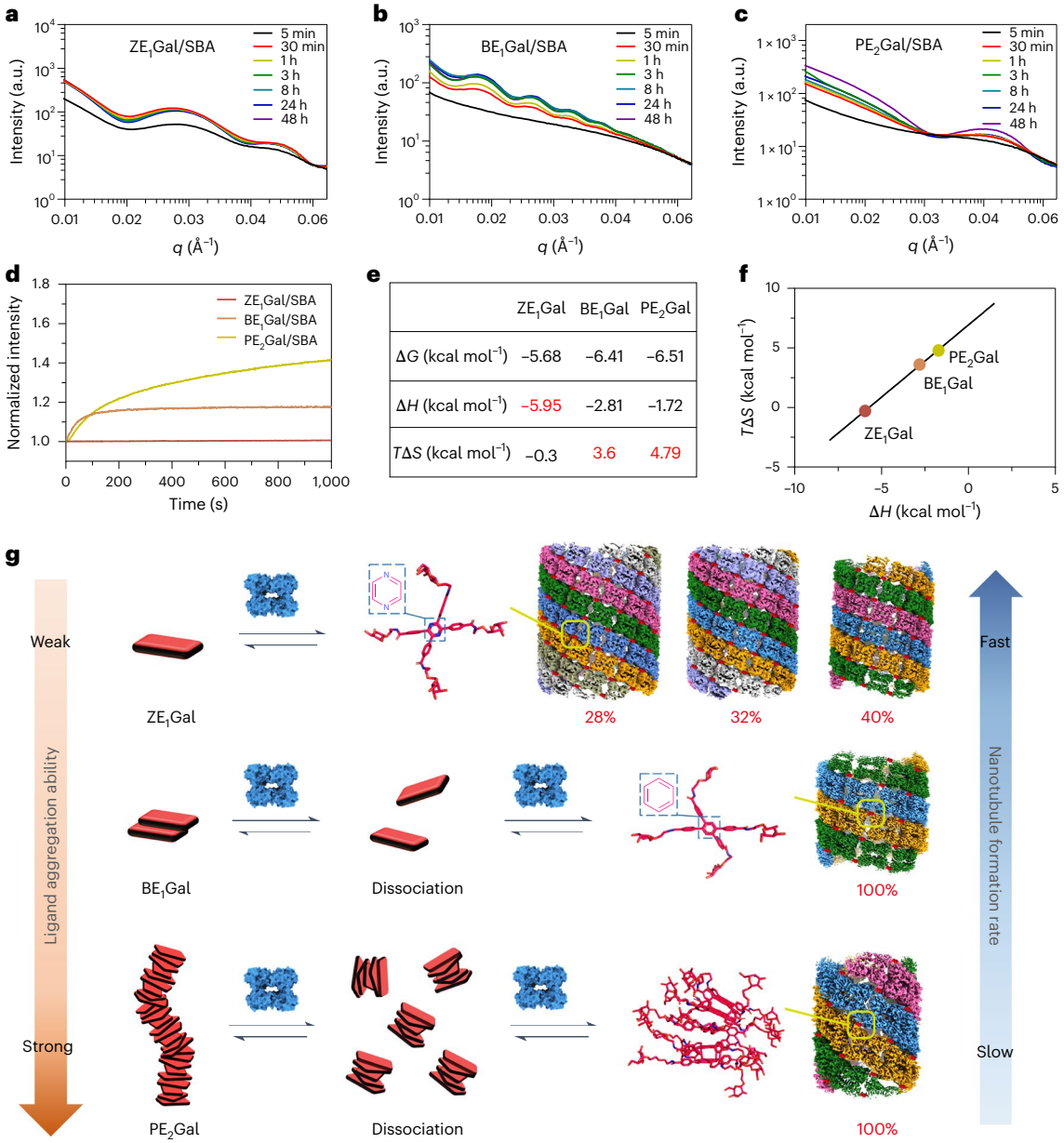

Fig. 5 | Kinetic and thermodynamic characterization of PSPs. a–**c**, SAXS spectra at different time points depicting the formation process of PSP induced by **ZE_1Gal** (**a**), **BE_1Gal** (**b**) and **PE_2Gal** (**c**). **d**, Fluorescence changes over time during the formation of PSP by three ligands. [ligands] = 160 μM, [SBA] = 20 μM. **e**, Isothermal titration calorimetry analysis of the thermodynamic parameters of process that ligands induced PSP. Temperature = 298 K. **f**, The plot displays the linear relationship between the enthalpy (ΔH) and entropy ($T\Delta S$) terms indicating the enthalpy–entropy compensation behaviour. **g**, A proposed scheme for regulating the PSPs by the ligand aggregation states; stronger aggregation ability of ligand resulted in a slower PSP rate. Meanwhile, the structure of protein nanotubules is homogenized in the sacrificial pathway.

The initial nucleation of the nanotubules through different assembly pathways was investigated by tracking of scattered light intensity. The protein supramolecular polymerization induced by these ligands was analysed in accordance with the homogeneous nucleated polymerization model[35]. Consistent with the SAXS tracking results, the fitting data of scattered light intensity indicated that the nucleation rate gradually decreased from **ZE_1Gal**, to **BE_1Gal** and to **PE_2Gal** because of the different aggregation states of the three ligands (Supplementary Fig. 50). The parameter n^*, which denotes the critical nucleus, exhibited the same trend as the nucleation rate[36]. The consistent trends of n^* and diameters of these protein nanotubules suggest that the nucleation process may determine the tubular diameters (Supplementary Fig. 51). Cryo-EM tracking confirmed that these ligands prompted SBA assembly into rings, followed by nanotubule growth through nucleation–elongation (Supplementary Fig. 52), which was similar to the growth model of native microtubules[37].

Isothermal titration calorimetry (ITC) was used to analyse the thermodynamic parameters of the process by which three ligands induce SBA to polymerize into nanotubules (Fig. 5e and Supplementary Fig. 53). First, the K_D values of **ZE_1Gal**, **BE_1Gal** and **PE_2Gal** were quite similar, indicating the retained binding ability of Gal to SBA in these three ligands. Their free energy change was similar, but a decrease trend of ΔG can be found from **ZE_1Gal** to **BE_1Gal** and then **PE_2Gal**. With the same type of Gal/SBA binding inducing nanotubule formation, which makes a similar contribution to ΔH, it was interesting to find that the ΔH of **ZE_1Gal** was around −5.95 kcal mol^{-1}, which is much greater than those of the other two ligands (**BE_1Gal** = −2.81 kcal mol^{-1} and **PE_2Gal** = −1.72 kcal mol^{-1}; Fig. 5e). More importantly, entropy changes

of **BE_1Gal** and **PE_2Gal** were much greater, with $T\Delta S$ values of 3.6 and 4.79 kcal mol^{-1}, respectively, whereas that of **ZE_1Gal** was −0.3 kcal mol^{-1} (Fig. 5e). These enthalpy–entropy changes correlate to each other since a linear relationship can be drawn between ΔH and $T\Delta S$ (Fig. 5f). These results indicated that there was substantial enthalpy–entropy compensation behaviour[38,39] in the cases of **BE_1Gal** and **PE_2Gal**, which can be attributed to the dissociation of the aggregated ligands during protein assembly (Fig. 5g). In other words, the fibrous structure of **PE_2Gal** itself dissociated into pentamers, which contributed to the great entropy gain measured by ITC, similar dissociation of **BE_1Gal** from oligomer to monomer enhanced the entropy as well. Based on the ITC results, we may conclude that **ZE_1Gal** rapidly induced protein nanotubules formation in its monomeric form, driven more by enthalpy. This fast growth of nanotubules would lead to kinetic trapping and result in microtubular structural polymorphism. In contrast, **BE_1Gal** disassembled from oligomers to monomers, which resulted in increased entropy. This provided time for nanotubules to become uniform structure. Similarly, for **PE_2Gal**, dissociation from fibrous assemblies to pentamers also led uniform diameter of the nanotubules. The results indicated that via disassembly of LSP, homogenization of helical protein nanotubules can be achieved in vitro, demonstrating a possible mechanism of uniform nanotubules in vivo and giving a bright future in human-made active materials.

Conclusion

In summary, the homogeneity of helical protein nanotubules was achieved by sacrifice of small-molecular supramolecular polymers. By designing molecular structure, the aggregation state of ligands was controlled to modulate the outcomes of the competition system, resulting in five protein nanotubules with different structures and protein arrangements. The competitive mechanism demonstrated that the dissociative ligand substantially contributes to the entropy change of the tube formation, unifies the protein tubular structure, which was only controlled by enthalpy with uncontrollable diameters and helical packings before. More importantly, the sacrifice of LSP to the generation of PSP not only substantially changed the solution property, but also induced the deformation of liposomes, demonstrating potential creation in protocell combined with other approach[40,41]. Such competition may be applicable to other supramolecular structures with proteins involved, which could be helpful for a deeper understanding of supramolecular competition phenomena in living systems. Considering the crucial role of natural microtubules as cytoskeleton, these results provide a bright future in constructing protocells with complex regulation on its behaviour via artificial cytoskeleton, shedding lights on design of artificial intelligent materials.

Methods

Materials

Commercial reagents were mainly obtained from J&K Scientific, Sigma-Aldrich, Innochem and Adamas-beta, and were used as received unless otherwise stated. 1,2-Dioleoyl-*sn*-glycero-3-phosphocholine (DOPC), cholesterol (ovine) and 1,2-dioleoyl-*sn*-glycero-3-phosphoethanolamine-*N*-(lissamine rhodamine B sulfonyl) (ammonium salt) (Rhod PE) were purchased from Avanti Lipids. Anhydrous *N*,*N*-dimethylformamide was purified using a solvent purification system (PS-MD3, Innovative Technology). Detailed synthetic procedures for ligands are given in the Supplementary Information. Soybean agglutinin protein and FITC-labelled SBA were purchased from Vector.

LSP and PSP preparation

To prepare the ligand sample, six ligands were dissolved in water at a concentration of 800 μM. Samples were sonicated for 30 min and equilibrated for 24 h. This procedure was applied to obtain reproducible experiments.

Protein assembly preparation: all self-assembly experiments were performed in the same HEPES buffer (Ca^{2+} = 250 μM, Mn^{2+} = 250 μM, HEPES = 300 μM, pH 7.2). Soybean agglutinin protein (lyophilized powder) was dissolved in buffer at a concentration of 40 μM (calculated as tetramer), and filtered through a Miliipore 0.45 μm membrane. Nanodrop was used to define the final concentration of SBA solution. All of the other ligands were dissolved in buffer at a concentration of 0.8 mM and filtered through a Millipore 0.45 μm membrane. The protein-assembly structure was prepared by mixing the ligand and protein solutions, and additional buffer, together to give a final ligand:protein molar ratio of 8:1. For example, if we wanted to obtain 100 μl **ZE_1Gal/SBA**, 20 μl **ZE_1Gal** solution (800 μM) and 50 μl SBA protein solution (40 μM), 30 μl buffer was mixed to achieve the above assembly environments. For other ligands, the self-assembly experiment was done in the same protocol. Unless otherwise stated, all measurements were conducted on samples prepared after 24 h.

Spectroscopic measurements

Dynamic light scattering was taken by Zeta sizer Nano ZS90 from Malvern Instruments. Solution-phase synchrotron SAXS experiment data were obtained on the SAXS beam line (BL16B1) of the Shanghai Synchrotron Radiation Facility. The incident X-ray wavelength was 0.124 nm. The sample-to-detector distance was 1.89 m. Scattering images recorded were integrated along the Debye–Scherrer ring using the FIT2D software[42], affording one-dimensional intensity data. Ultraviolet–visible absorption spectra were recorded using a Shimadzu UV2550 spectrophotometer. The fluorescence emission spectra of the samples were recorded on an Edinburgh FLS1000. Circular dichroism spectra were recorded on a Chirascan spectrometer (Applied Photophysics). Diffusing-wave spectra were recorded on the LS Instruments DWS RheoLab III at 20 °C, using a transmission measurement mode. The tracer particles were 500 nm polystyrene particles.

Small-angle neutron scattering experiments were performed using the very small-angle neutron scattering instrument BL-14 (ref. 43) at the China Spallation Neutron Source. Neutron data were collected with a wavelength range from 2.2 Å to 6.7 Å, employing a collimation length of 9.92 m. Samples were encased in quartz cells with an optical path length of 1 mm. Data reduction was performed using the direct beam method[43], which included measurement of the direct beam, solid angle and transmission correction as well as solvent scattering background subtraction.

Molecular dynamics simulations

The small organic molecule was parameterized using the CHARMM General Force Field (CGenFF) program[44]. GROMACS 2018 was employed for all of the molecular dynamics simulations[45]. The simulation box size was designed to be10 nm × 10 nm × 10 nm, and ten small molecules were stochastically generated in the box by using the insert-molecules command. For the fibre structures, the simulation box size was designed as 10 nm × 10 nm × 8 nm. The CHARMM36 force field was used for the molecules and TIP3P model for explicit water molecules[46,47]. The particle mesh Ewald method[48] was used to calculate the electrostatic interactions of the system with a grid spacing of 1.75 Å, while short-ranged electrostatic and Van der Waals interactions were truncated at 1.2 nm. The system was first minimized with harmonic restraints of 200 kJ mol^{-1} Å^{-2} placed on all heavy atom of the solute molecule. The reference temperature was maintained at 298 K by the stochastic integrator with a relaxation time at 2 ps. The pressure was maintained at 1.0 bar by the Berendsen algorithm with a relaxation time of 1 ps. The system composed of the small molecules, and water was pre-equilibrated in the NVT ensemble for 500 ps and another 500 ps in the NPT ensemble, by using a V-rescale thermostat and Parrinello–Rahman(6) barostat, respectively. The production run was then continued for another 100 ns. An integration time-step at 1 fs was used for all of the above simulations. The SASA results of the

clusters, as well as the distance and angle between two pyrenes, were obtained by using the sasa, distance and gangle codes in GROMACS 2018 with default parameters.

Cryo-EM data collection and processing

Cryo-EM imaging was performed using a JEOL Cryo ARM 300 TEM equipped with a cold field emission gun operating at 300 kV and a Gatan K3 direct electron detector. The cryo-EM specimens were prepared as follows: an aliquot (~3.5 µl) of sample solution was placed on a glow-discharged holey carbon-film-coated copper grid (Quantifoil Cu 200 mesh, R1.2/1.3); the samples were blotted for 3 s with filter paper from both sides at ~100% humidity and 4 °C with a FEI Vitrobot rapid-plunging device and then flash-frozen in liquid ethane cooled by liquid nitrogen. Vitrified grids were either transferred directly to the microscope cryo-holder or stored in liquid nitrogen before imaging. For 3D reconstruction images collection, the images were automatically collected using SerialEM and a preset defocus range 0.5–3 µm at a magnification of 50,000 (Raw pixel size is 0.48 Å) under a total exposure dose of 50 e^{-} $Å^{-2}$ for each movie stack containing 40 frames.

All of the procedures for image processing were performed using CryoSPARC[49,50]. A total of 4306, 5371 and 2386 images, for **ZE_1Gal/SBA**, **BE_1Gal/SBA** and **PE_2Gal/SBA** complex samples respectively, were first operate patch motion correction, and then patch CTF estimation. Using filament tracer process to track nanotubules and extract the particles from micrographs. As a result, a total of 305908, 329591 and 228059 particles were selected and then extracted with a box size of 750, 500 and 400 pixels in case of **ZE_1Gal/SBA, BE_1Gal/SBA** and **PE_2Gal/SBA** respectively. In two-dimensional (2D) class, we selected the fine 2D class particles and exercised the helical refinement. The symmetry search was also done. For the **ZE_1Gal/SBA** case, category 1 nanotubules (12-7) have helical twist of 23.92°, helical rise of 35.55 Å and the point group symmetry is D_1. Category 2 (11–6)/category 3 (10–4) nanotubules induced by **ZE_1Gal**, the helical twist is −27.06°/−42.35°, helical rise of 33.73 Å/38.18 Å and the point group symmetry is D_1/D_2. In the case of **BE_1Gal/SBA** (9–3), the helical twist, helical rise and point group symmetry are −10.59°, 63.65 Å and D_3. In the case of **PE_2Gal/SBA** (6–4), the helical twist, helical rise and point group symmetry are 43.53°, 41.06 Å and D_2. And the final resolution of the **ZE_1Gal/SBA** is 4.43 Å (12–7), 4.26 Å (11–6) and 3.97 Å (10–4). The resolution of **BE_1Gal/SBA** (9–3) is 3.13 Å and **PE_2Gal/SBA** (6–4) is 3.57 Å. This overall resolution estimate was based on the gold-standard Fourier shell correlation 0.143 criterion[51]. All the images of 3D reconstructions were prepared with UCSF ChimeraX[52].

Model building and refinement

Model building was performed based on the 3.13–4.43 Å post-processing map. The coordinates of SBA tetramer (PDB accession no. 1SBE) were first roughly fitted into the electron microscopy density map by UCSF Chimera. Individual monomers within the tetramer were then locally fitted into the density to maximize the correlation between the model and map, and then manually refined in Coot[53].

Liposome encapsulated ligand/protein preparation

Liposome were prepared according to literature works[54,55]. Briefly, lipids mix solubilized in chloroform were prepared and desiccated using a gentle nitrogen flow. After that, the vial was brought inside a glovebox, where the lipid film was resuspended in 500 µl of chloroform. The chloroform in the lipid solution was then evaporated under vacuum for at least 2 h. A mixture of 2 ml silicon oil (viscosity 5 cSt (25 °C), Sigma-Aldrich) and 0.5 ml mineral oil (BioReagent, Sigma-Aldrich) was then added dropwise to the lipids while vortexing. The resulting suspension was sonicated in ice for 15 min. The lipids mix used in this study was composed of DOPC (70.4% mol/mol), cholesterol (29.32% mol/mol) and Rhod PE (0.28% mol/mol). Finally, droplets were generated by pipetting 10 µl 'inner' aqueous solution (ligand induced protein assembly solution) into 50 µl lipid-in-oil suspension. The tube was flicked until solution turbid, left to stand at room temperature for 5 min and then flicked again ten times until turbid.

A mask of the liposome was obtained by thresholding the fluorescence intensity of fluorescently labelled lipid at the pane of the liposome and an ellipse was fitted to the mask in ImageJ[56]. The eccentricity of the fitted ellipse was calculated as, where M and m are the major and minor axis of the ellipse:

$$e = \sqrt{1 - \frac{m^2}{M^2}}$$

Data availability

All data required to interpret, verify and extend the results are given in the paper and its Supplementary Information. The maps of nanotubules are deposited in the Electron Microscopy Data Bank under accession codes EMD-60193, EMD-60194 and EMD-60195 for **ZE_1Gal/SBA**, EMD-60192 for **BE_1Gal/SBA** and EMD-60191 for **PE_2Gal/SBA**.

References

1. Lutz, J.-F., Lehn, J.-M., Meijer, E. W. & Matyjaszewski, K. From precision polymers to complex materials and systems. *Nat. Rev. Mater.* **1**, 16024 (2016).
2. Rest, C., Kandanelli, R. & Fernández, G. Strategies to create hierarchical self-assembled structures via cooperative non-covalent interactions. *Chem. Soc. Rev.* **44**, 2543–2572 (2015).
3. Johnson, S. et al. Molecular structure of the intact bacterial flagellar basal body. *Nat. Microbiol.* **6**, 712–721 (2021).
4. Bieling, P. et al. Reconstitution of a microtubule plus-end tracking system in vitro. *Nature* **450**, 1100–1105 (2007).
5. Kollman, J. M., Polka, J. K., Zelter, A., Davis, T. N. & Agard, D. A. Microtubule nucleating γ-TuSC assembles structures with 13-fold microtubule-like symmetry. *Nature* **466**, 879–882 (2010).
6. von der Ecken, J. et al. Structure of the F-actin–tropomyosin complex. *Nature* **519**, 114–117 (2015).
7. Kollman, J. M., Merdes, A., Mourey, L. & Agard, D. A. Microtubule nucleation by γ-tubulin complexes. *Nat. Rev. Mol. Cell Biol.* **12**, 709–721 (2011).
8. Gudimchuk, N. B. & McIntosh, J. R. Regulation of microtubule dynamics, mechanics and function through the growing tip. *Nat. Rev. Mol. Cell Biol.* **22**, 777–795 (2021).
9. Brouhard, G. J. & Rice, L. M. Microtubule dynamics: an interplay of biochemistry and mechanics. *Nat. Rev. Mol. Cell Biol.* **19**, 451–463 (2018).
10. Weingarten, M. D., Lockwood, A. H., Hwo, S. Y. & Kirschner, M. W. A protein factor essential for microtubule assembly. *Proc. Natl Acad. Sci. USA* **72**, 1858–1862 (1975).
11. Kellogg, E. H. et al. Near-atomic model of microtubule–tau interactions. *Science* **360**, 1242–1246 (2018).
12. Alonso, A. C., Grundke-Iqbal, I. & Iqbal, K. Alzheimer's disease hyperphosphorylated tau sequesters normal tau into tangles of filaments and disassembles microtubules. *Nat. Med.* **2**, 783–787 (1996).
13. Malay, A. D. et al. An ultra-stable gold-coordinated protein cage displaying reversible assembly. *Nature* **569**, 438–442 (2019).
14. Šimić, G. et al. Tau protein hyperphosphorylation and aggregation in Alzheimer's disease and other tauopathies, and possible neuroprotective strategies. *Biomolecules* **6**, 6 (2016).
15. Otsuka, C. et al. Supramolecular polymer polymorphism: spontaneous helix–helicoid transition through dislocation of hydrogen-bonded π-Rosettes. *J. Am. Chem. Soc.* **145**, 22563–22576 (2023).
16. Sarkar, A., Dhiman, S., Chalishazar, A. & George, S. J. Visualization of stereoselective supramolecular polymers by chirality-controlled energy transfer. *Angew. Chem. Int. Ed.* **129**, 13955–13959 (2017).

17. Bi, Y. et al. Controlled hierarchical self-assembly of nanoparticles and chiral molecules into tubular nanocomposites. *J. Am. Chem. Soc.* **145**, 8529–8539 (2023).
18. Wang, J. et al. Nucleation-controlled polymerization of nanoparticles into supramolecular structures. *J. Am. Chem. Soc.* **135**, 11417–11420 (2013).
19. Biswas, S. et al. A tubular biocontainer: metal ion-induced 1D assembly of a molecularly engineered chaperonin. *J. Am. Chem. Soc.* **131**, 7556–7557 (2009).
20. Miranda, F. F. et al. A self-assembled protein nanotube with high aspect ratio. *Small* **5**, 2077–2084 (2009).
21. Luo, Q., Hou, C., Bai, Y., Wang, R. & Liu, J. Protein assembly: versatile approaches to construct highly ordered nanostructures. *Chem. Rev.* **116**, 13571–13632 (2016).
22. Vantomme, G. & Meijer, E. W. The construction of supramolecular systems. *Science* **363**, 1396–1397 (2019).
23. Mattia, E. & Otto, S. Supramolecular systems chemistry. *Nat. Nanotechnol.* **10**, 111–119 (2015).
24. Ślęczkowski, M. L., Mabesoone, M. F. J., Ślęczkowski, P., Palmans, A. R. A. & Meijer, E. W. Competition between chiral solvents and chiral monomers in the helical bias of supramolecular polymers. *Nat. Chem.* **13**, 200–207 (2021).
25. Tamaki, K. et al. Photoresponsive supramolecular polymers capable of intrachain folding and interchain aggregation. *J. Am. Chem. Soc.* **146**, 22166–22171 (2024).
26. Su, L. et al. Dilution-induced gel-sol-gel-sol transitions by competitive supramolecular pathways in water. *Science* **377**, 213–218 (2022).
27. Lehn, J.-M. Perspectives in chemistry—steps towards complex matter. *Angew. Chem. Int. Ed.* **52**, 2836–2850 (2013).
28. Li, Z. et al. Chemically controlled helical polymorphism in protein tubes by selective modulation of supramolecular interactions. *J. Am. Chem. Soc.* **141**, 19448–19457 (2019).
29. de Halleux, V. et al. 1,3,6,8-Tetraphenylpyrene derivatives: towards fluorescent liquid-crystalline columns? *Adv. Funct. Mater.* **14**, 649–659 (2004).
30. Vybornyi, M. et al. Formation of two-dimensional supramolecular polymers by amphiphilic pyrene oligomers. *Angew. Chem. Int. Ed.* **52**, 11488–11493 (2013).
31. Hendrikse, S. I. S. et al. Elucidating the ordering in self-assembled glycocalyx mimicking supramolecular copolymers in water. *J. Am. Chem. Soc.* **141**, 13877–13886 (2019).
32. Gupta, D., Cho, M., Cummings, R. D. & Brewer, C. F. Thermodynamics of carbohydrate binding to galectin-1 from Chinese hamster ovary cells and two mutants. A comparison with four galactose-specific plant lectins. *Biochemistry* **35**, 15236–15243 (1996).
33. Concellón, A., Lu, R.-Q., Yoshinaga, K., Hsu, H.-F. & Swager, T. M. Electric-field-induced chirality in columnar liquid crystals. *J. Am. Chem. Soc.* **143**, 9260–9266 (2021).
34. Figueira-Duarte, T. M. & Müllen, K. Pyrene-based materials for organic electronics. *Chem. Rev.* **111**, 7260–7314 (2011).
35. Meisl, G. et al. Molecular mechanisms of protein aggregation from global fitting of kinetic models. *Nat. Protoc.* **11**, 252–272 (2016).
36. Xia, H. et al. Supramolecular assembly of comb-like macromolecules induced by chemical reactions that modulate the macromolecular interactions in situ. *J. Am. Chem. Soc.* **139**, 11106–11116 (2017).
37. Akhmanova, A. & Kapitein, L. C. Mechanisms of microtubule organization in differentiated animal cells. *Nat. Rev. Mol. Cell Biol.* **23**, 541–558 (2022).
38. Breiten, B. et al. Water networks contribute to enthalpy/entropy compensation in protein–ligand binding. *J. Am. Chem. Soc.* **135**, 15579–15584 (2013).
39. Rekharsky, M. & Inoue, Y. Chiral recognition thermodynamics of β-Cyclodextrin: the thermodynamic origin of enantioselectivity and the enthalpy–entropy compensation effect. *J. Am. Chem. Soc.* **122**, 4418–4435 (2000).
40. Guindani, C., da Silva, L. C., Cao, S., Ivanov, T. & Landfester, K. Synthetic cells: from simple bio-inspired modules to sophisticated integrated systems. *Angew. Chem. Int. Ed.* **61**, e202110855 (2022).
41. Gao, N. & Mann, S. Membranized coacervate microdroplets: from versatile protocell models to cytomimetic materials. *Acc. Chem. Res.* **56**, 297–307 (2023).
42. Kimanius, D., Forsberg, B. O., Scheres, S. H. & Lindahl, E. Accelerated cryo-EM structure determination with parallelisation using GPUs in RELION-2. *eLife* **5**, e18722 (2016).
43. Zuo, T. et al. The multi-slit very small angle neutron scattering instrument at the China Spallation Neutron Source. *J. Appl. Crystallogr.* **57**, 380–391 (2024).
44. Vanommeslaeghe, K. et al. CHARMM general force field: a force field for drug-like molecules compatible with the CHARMM all-atom additive biological force fields. *J. Comput. Chem.* **31**, 671–690 (2010).
45. Van Der Spoel, D. et al. GROMACS: fast, flexible, and free. *J. Comput. Chem.* **26**, 1701–1718 (2005).
46. Guvench, O. et al. CHARMM additive all-atom force field for carbohydrate derivatives and its utility in polysaccharide and carbohydrate–protein modeling. *J. Chem. Theory Comput.* **7**, 3162–3180 (2011).
47. Jorgensen, W. L. & Madura, J. D. Quantum and statistical mechanical studies of liquids. 25. Solvation and conformation of methanol in water. *J. Am. Chem. Soc.* **105**, 1407–1413 (1983).
48. Darden, T., York, D. & Pedersen, L. Particle mesh Ewald: an *N*·log(*N*) method for Ewald sums in large systems. *J. Chem. Phys.* **98**, 10089–10092 (1993).
49. Punjani, A., Rubinstein, J. L., Fleet, D. J. & Brubaker, M. A. cryoSPARC: algorithms for rapid unsupervised cryo-EM structure determination. *Nat. Methods* **14**, 290–296 (2017).
50. Zivanov, J., Nakane, T. & Scheres, S. H. W. Estimation of high-order aberrations and anisotropic magnification from cryo-EM data sets in RELION-3.1. *IUCrJ* **7**, 253–267 (2020).
51. Rosenthal, P. B. & Henderson, R. Optimal determination of particle orientation, absolute hand, and contrast loss in single-particle electron cryomicroscopy. *J. Mol. Biol.* **333**, 721–745 (2003).
52. Pettersen, E. F. et al. UCSF ChimeraX: structure visualization for researchers, educators, and developers. *Protein Sci.* **30**, 70–82 (2021).
53. Emsley, P., Lohkamp, B., Scott, W. G. & Cowtan, K. Features and development of Coot. *Acta Crystallogr. D* **66**, 486–501 (2010).
54. De Franceschi, N., Barth, R., Meindlhumer, S., Fragasso, A. & Dekker, C. Dynamin A as a one-component division machinery for synthetic cells. *Nat. Nanotechnol.* **19**, 70–76 (2024).
55. De Franceschi, N. et al. Synthetic membrane shaper for controlled liposome deformation. *ACS Nano* **17**, 966–978 (2023).
56. Schneider, C. A., Rasband, W. S. & Eliceiri, K. W. NIH Image to ImageJ: 25 years of image analysis. *Nat. Methods* **9**, 671–675 (2012).

Acknowledgements

G.C. and L.L. thank NSFC/China (grant nos. 52125303, 52403179, and 92356305 and 22431002), the National Key Research and Development Program of China (grant no. 2023YFA0915300) and Innovation Program of Shanghai Municipal Education Commission (grant no. 2023ZKZD02) for financial support. M.L. thanks NSFC/China (grant nos. 92156023 and 92356306) for financial support.
This research is also supported by the Postdoctoral Fellowship Program of CPSF under grant no. GZC20240273. We thank the

Shanghai Synchrotron Radiation Facility (Bio-SAXS: BL19U2) for the SAXS test. We also thank the Spallation Neutron Source Science Center in Dongguan for neutron scattering experiments with the help of H. Cheng, T. Zuo, H. Zhu and X. Liu.

Author contributions

L.Y., L.L. and G.C. conceptualized and administered the project and wrote the paper. L.Y. performed the synthesis of all the ligands and studied the self-assembly of ligands and protein by spectroscopy experiments. L.L. performed the molecular dynamics simulations. L.Y. and X.D. performed the cryo-EM experiment. L.L. performed the cryo-EM images processing, model building and refinement. C.W. performed the microfluidics experiment. Y.L. and M.L. analysed and interpreted the results, and involved in revision of the paper.

Competing interests

The authors declare no competing interests.

Additional information

Supplementary information The online version contains supplementary material available at https://doi.org/10.1038/s44160-024-00726-y.

Correspondence and requests for materials should be addressed to Long Li or Guosong Chen.

Peer review information *Nature Synthesis* thanks Huaimin Wang, Shiki Yagai and the other, anonymous, reviewer(s) for their contribution to the peer review of this work. Primary Handling Editor: Alison Stoddart, in collaboration with the *Nature Synthesis* team.